Cardiac magnetic source imaging based on current multipole model*

Tang Fa-Kuan(唐发宽)[a], Wang Qian(王 倩)[a)b)], Hua Ning(华 宁)[a)], Lu Hong(陆 宏)[a)], Tang Xue-Zheng(唐雪正)[a)], and Ma Ping(马 平)[b)†]

[a)] *Department of Cardiology, The 309th Hospital of PLA, Beijing* 100091, *China*
[b)] *Department of Physics, State Key Laboratory for Artificial Microstructure and Mesoscopic Physics, Peking University, Beijing* 100871, *China*

(Received 23 May 2010; revised manuscript received 4 August 2010)

It is widely accepted that the heart current source can be reduced into a current multipole. By adopting three linear inverse methods, the cardiac magnetic imaging is achieved in this article based on the current multipole model expanded to the first order terms. This magnetic imaging is realized in a reconstruction plane in the centre of human heart, where the current dipole array is employed to represent realistic cardiac current distribution. The current multipole as testing source generates magnetic fields in the measuring plane, serving as inputs of cardiac magnetic inverse problem. In the heart-torso model constructed by boundary element method, the current multipole magnetic field distribution is compared with that in the homogeneous infinite space, and also with the single current dipole magnetic field distribution. Then the minimum-norm least-squares (MNLS) method, the optimal weighted pseudoinverse method (OWPIM), and the optimal constrained linear inverse method (OCLIM) are selected as the algorithms for inverse computation based on current multipole model innovatively, and the imaging effects of these three inverse methods are compared. Besides, two reconstructing parameters, residual and mean residual, are also discussed, and their trends under MNLS, OWPIM and OCLIM each as a function of SNR are obtained and compared.

Keywords: cardiac magnetic imaging, current multipole, heart-torso model, inverse method
PACS: 07.05Tp, 87.80.–y, 87.85.–d **DOI:** 10.1088/1674-1056/20/1/010702

1. Introduction

Magnetocardiography (MCG) is a non-invasive, non-contact imaging modality based on external measurements of cardiac magnetic fields produced by bioelectric currents within the heart. By utilizing superconductivity quantum interference device (SQUID), the weak cardiac magnetic signals are recorded and used to form MCG maps.[1−3] Although the magnetic imaging using MCG has a lower resolution than transmission tomography (CT) and magnetic resonance imaging (MRI), it can provide functional images which are helpful for diagnosing many diseases, such as Wolff–Parkinson–White (WPW) syndrome, infarction, atrial and ventricular overload, *etc.*

Unfortunately, the cardiac current source estimation is a severely ill-posed inverse problem. Most approaches used to solve this inverse problem can be classified into two kinds: imaging and parametric methods. The first method needs to tessellate current source area into many small parts, assign an elemental current source to each area element, relate source elements to measuring elements by geometrical matrix and then solve matrix-formed inverse problem without iteration.[4,5] The second method is to adopt a functional model and use several parameters to represent bioelectric sources. The most typical and classic cardiac functional model is the equivalent current dipole (ECD) model[6] and multiple current dipole model.[7] While their localization errors may increase with the source extension and the use of multipole expansion can help deal with this problem, so there comes the current multipole model.[8,9] The current multipole expression can be obtained by using current multipole expansions (CME) and magnetic multipole expansion (MME) in spherical or Cartesian coordinate system.

As to the first source estimating method, researchers usually suppose that each elemental current source, which is usually chosen to be a current dipole, has a definite position but an undefined magnitude

*Project supported by the State Key Development Program for Basic Research of China (Grant No. 2006CB601007), the National Natural Science Foundation of China (Grant No. 10674006), and the National High Technology Research and Development Program of China (Grant No. 2007AA03Z238).
†Corresponding author. E-mail: maping@pku.edu.cn
© 2011 Chinese Physical Society and IOP Publishing Ltd

and orientation, so in this case the magnetic field is a linear function of the current distribution. Some linear methods are suitable for solving this inverse problem, such as maximum-likelihood (ML) method,[10] minimum-norm least-squares (MNLS) method, optimal weighted pseudo-inverse method (OWPIM),[11] minimum mean-square error (MMSE) method,[12] optimal constrained linear inverse method (OCLIM),[13] *etc.* When it comes to the parametric methods, functional current sources' position, magnitude and orientation are all indefinite, while these unknown parameters can be found by a least-square fit to the observed measurements.[14] The simulated annealing algorithm, genetic algorithm, Nelder–Mead algorithm, *etc.* are usually used to fit calculated data to realistic observed data. However, because this is a nonlinear inverse problem and iterative solution is required, these algorithms are computationally expensive.

In this article, the current multipole expanded to the first order terms is chosen as a testing cardiac source aiming at exciting simulated magnetic fields in the measuring plane. Depending on these magnetic data, current dipole array reconstruction is realized by MNLS (or Moore–Penrose), OWPIM and OCLIM inverse computations of the forward matrix and how random noises have an influence on current dipole imaging effect is also discussed.

2. Methods

For a bounded conductor G divided into homogeneous subregions G_j by surfaces S_j, $j = 1, 2, \ldots, n$, the representation for magnetic field $\boldsymbol{B}$ in terms of bioelectric current $\boldsymbol{J}^i$ and the values of electric potential V on S_j can be given as:[15]

$$\boldsymbol{B}(\boldsymbol{r}) = \boldsymbol{B}_0(\boldsymbol{r}) + \frac{\mu_0}{4\pi}\sum_{j=1}^{n}(\sigma_j' - \sigma_j'') \times \int_{S_j} V(\boldsymbol{r}')\frac{\boldsymbol{r}-\boldsymbol{r}'}{|\boldsymbol{r}-\boldsymbol{r}'|^3} \times \boldsymbol{n}_j \,\mathrm{d}S_j, \quad (1)$$

where

$$\boldsymbol{B}_0(\boldsymbol{r}) = \frac{\mu_0}{4\pi}\int_G \boldsymbol{J}^i(\boldsymbol{r}') \times \frac{\boldsymbol{r}-\boldsymbol{r}'}{|\boldsymbol{r}-\boldsymbol{r}'|^3}\,\mathrm{d}v' \quad (2)$$

is the magnetic induction generated by $\boldsymbol{J}^i$ in a homogeneous unbounded space, σ_j' and σ_j'' are conductivities on the inner and the outer sides of S_j, and $\boldsymbol{n}_j$ is the outer unit normal of the surface S_j.

$\boldsymbol{B}_0(\boldsymbol{r})$ can be expanded using multipole expansion of the dyadic Green's function about the centroid of bioelectric currents $\boldsymbol{r}_0$ in Cartesian coordinate system[16] as follows:

$$\begin{aligned}
&\boldsymbol{B}_0(\boldsymbol{r}) \\
&= \frac{\mu_0}{4\pi}\Bigg[A_{10}\frac{\boldsymbol{e}_z\times\boldsymbol{r}}{r^3} + A_{11}\frac{\boldsymbol{e}_x\times\boldsymbol{r}}{r^3} + B_{11}\frac{\boldsymbol{e}_y\times\boldsymbol{r}}{r^3} \\
&\quad + A_{20}\frac{3z(\boldsymbol{e}_z\times\boldsymbol{r})}{2r^5} + A_{21}\frac{3(z\boldsymbol{e}_x + x\boldsymbol{e}_z)\times\boldsymbol{r}}{2r^5} \\
&\quad + B_{21}\frac{3(z\boldsymbol{e}_y + y\boldsymbol{e}_z)\times\boldsymbol{r}}{2r^5} \\
&\quad + A_{22}\frac{3(x\boldsymbol{e}_x - y\boldsymbol{e}_y)\times\boldsymbol{r}}{r^5} + B_{22}\frac{3(y\boldsymbol{e}_x + x\boldsymbol{e}_y)\times\boldsymbol{r}}{r^5} \\
&\quad + \alpha_{10}\frac{3z\boldsymbol{r} - r^2\boldsymbol{e}_z}{r^5} + \alpha_{11}\frac{3x\boldsymbol{r} - r^2\boldsymbol{e}_x}{r^5} \\
&\quad + \beta_{11}\frac{3y\boldsymbol{r} - r^2\boldsymbol{e}_y}{r^5} + \ldots\Bigg], \quad (3)
\end{aligned}$$

where $\boldsymbol{e}_x, \boldsymbol{e}_y, \boldsymbol{e}_z$ are the unit vectors along the axes x, y and z. The first three terms denote the current dipole, dipole moment $\boldsymbol{p} = (A_{11}, B_{11}, A_{10})$, and the last three terms before the ellipsis are associated with the magnetic dipole, magnetic dipole moment $\boldsymbol{m} = (\alpha_{11}, \beta_{11}, \alpha_{10})$, and the five terms in the middle result from the current quadrupole, five elements of current quadrupole tensor $(A_{20}, A_{21}, B_{21}, A_{22}, B_{22})$. For simplicity, $\boldsymbol{r} - \boldsymbol{r}_0$ is replaced by $\boldsymbol{r}$ in Eq. (3).

Current multipole has been deemed as a kind of cardiac functional model, especially in QRS and ST-T complex during one cardiac cycle. The current multipole, as an alternative model of equivalent current dipole (ECD), is suitable for simulating sources with significant spatial extent and arbitrary activation patterns. Although the higher order terms of current multipole expansion can provide a more accurate modification to cardiac current source, the current multipole expanded to the first order terms is enough for characterizing electrophysiological activities of human heart generally. As shown in Eq. (3), this cardiac source model is composed of three parts: the current dipole, the magnetic dipole, and the current quadrupole. If the magnetic signals are detected along the z axis, some parameters in Eq. (3) will disappear and $B_{0,z}$ can be expressed as

$$\begin{aligned}
&B_{0,z} \\
&= \frac{\mu_0}{4\pi}\Bigg[A_{11}\frac{y-y_0}{|r-r_0|^3} - B_{11}\frac{x-x_0}{|r-r_0|^3} \\
&\quad + A_{21}\frac{3(y-y_0)(z-z_0)}{2\,|r-r_0|^5} - B_{21}\frac{3(x-x_0)(z-z_0)}{2\,|r-r_0|^5} \\
&\quad + A_{22}\frac{6(x-x_0)(y-y_0)}{|r-r_0|^5}
\end{aligned}$$

$$+ B_{22}\frac{3[(y-y_0)^2-(x-x_0)^2]}{|r-r_0|^5} + \alpha_{10}\frac{3(z-z_0)^2-|r-r_0|^2}{|r-r_0|^5} + \alpha_{11}\frac{3(x-x_0)(z-z_0)}{|r-r_0|^5} + \beta_{11}\frac{3(y-y_0)(z-z_0)}{|r-r_0|^5}\Big]. \quad (4)$$

Since the second term on the right-hand side of Eq. (1), which arises from surface current $-(\sigma_j' - \sigma_j'')V(\boldsymbol{r}')\boldsymbol{n}_j(\boldsymbol{r}')$, can change the distribution of magnetic field $\boldsymbol{B}_0$, the boundary effect of piecewise conductor should be considered, so we use the boundary element method (BEM) to solve that. The BEM based on the ideas of Barr *et al.*[17] is a kind of node-to-node tessellating method in which surfaces are divided into many small triangles and each node of these triangles is connected by geometrical matrix. As a result, the electric potentials on each surface and the magnetic fields outside the conductor can be calculated from electric potentials in an unbounded homogeneous space. This method is suited for settling forward problems of cardiac magnetic fields and electric potentials.

The output of a magnetometer or magnetic-gradiometer B_k at observation point $\boldsymbol{r}_k$ is linearly related to the bioelectric current distribution, thus there will exist a vector field $\boldsymbol{L}_k(\boldsymbol{r}')$, called lead field, satisfying:[18]

$$B_k = \int_G \boldsymbol{L}_k(\boldsymbol{r}')\cdot\boldsymbol{J}^i(\boldsymbol{r}')\mathrm{d}v', \quad k=1,2,\ldots,M, \quad (5)$$

where $\boldsymbol{L}_k(\boldsymbol{r}')$ is concerned only with the geometries of current sources and the distributions of magnetic observation points.

At the same time, assume that BEM tessellates surface S into N_{SD} triangles, thus B_k can be expressed in the form of linear combination of electric potentials (in unbounded space) on the centroids of each triangle on S[19] as follows:

$$B_k = B_{0,k} + \sum_S \sum_{m_S=1}^{N_{\mathrm{SD}}} A^{\mathrm{S}}_{km_S} V^{\mathrm{S}}_{0,m_S}, \quad k=1,2,\cdots,M, \quad (6)$$

where the first summation of the second term on the right-hand side runs over all surfaces. Matrix $\boldsymbol{A}^S$ $(M\times N_{\mathrm{SD}})$ consists of geometrical factors and is computed only once.

Comparing Eq. (5) with Eq. (6), we obtain

$$\boldsymbol{L}_k(\boldsymbol{r}') = \boldsymbol{L}_{0,k}(\boldsymbol{r}') + \sum_S \sum_{m_S}^{N_{\mathrm{SD}}} A^{\mathrm{S}}_{km_S}\boldsymbol{L}^{\mathrm{E}}_{0,m_S}(\boldsymbol{r}'), \quad (7)$$

where

$$\boldsymbol{L}_{0,k}(\boldsymbol{r}') = \frac{\mu_0}{4\pi}\frac{(\boldsymbol{r}_k-\boldsymbol{r}')\times\boldsymbol{e}_k}{|\boldsymbol{r}_k-\boldsymbol{r}'|^3}$$

and

$$\boldsymbol{L}^{\mathrm{E}}_{0,m_S}(\boldsymbol{r}') = \frac{1}{4\pi\sigma}\frac{\boldsymbol{r}_{m_S}-\boldsymbol{r}'}{|\boldsymbol{r}_{m_S}-\boldsymbol{r}'|^3}$$

are the lead field and the electric lead field without consideration of boundary effect, μ_0 is the permeability in vacuum, σ represents the conductivity in homogeneous infinite space, and $\boldsymbol{r}_{m_S}$ is the m_sth observation point of electric potential on surface S.

We suppose that the cardiac current source can be simplified into a set of current dipoles distributed evenly in the thin source plane in the centre of heart, forming a current dipole array and this simplified cardiac source model has been used[4,5] to realize the magnetic imaging of bioelectric currents. The source plane that is assumed to be coincident with the imaging plane is divided into grids, and in the middle of each grid element there lies a current dipole with an undefined magnitude and orientation. Our aim is to reconstruct these current dipoles in the imaging plane based on the simulated cardiac magnetic data.

However, why can the cardiac current source be reduced into a current dipole array? If the source plane S' with thickness h is tessellated into N ($N = n\times n$) grid and $\boldsymbol{r}_j{}'$ denotes the position of the jth current dipole in the centre of the jth cell $\Delta S_j'$, Eq. (5) can be rewritten as

$$B_k = \sum_{j=1}^{N}\boldsymbol{L}_k(\boldsymbol{r}_j{}')\cdot\boldsymbol{J}(\boldsymbol{r}_j{}')h\Delta S_j', \quad (8)$$

where $\boldsymbol{J}(\boldsymbol{r}_j')h\Delta S_j'$ in dimension of A · m could be regarded as a current dipole $\boldsymbol{Q}_j = (Q_{j,x}, Q_{j,y}, Q_{i,z})^{\mathrm{T}}$, so in this sense the current dipole array is an appropriate equivalent current source model of heart.

As to all the magnetic fields B detected at M measuring grid nodes and all the current dipoles, i.e., $\boldsymbol{B} = (B_1, B_2, \ldots, B_M)^{\mathrm{T}}$ and $\boldsymbol{Q} = (\boldsymbol{Q}_1, \boldsymbol{Q}_2, \ldots, \boldsymbol{Q}_N)^{\mathrm{T}}$, according to Eq. (8), they are connected by lead field matrix $\boldsymbol{L}$ $(M\times N)$ and satisfy:

$$\boldsymbol{B} = \boldsymbol{L}\boldsymbol{Q}. \quad (9)$$

In Eq. (9) the influences from various kinds of noises are not taken into consideration. For realistic case, noises should not be ignored, so we have

$$\boldsymbol{B} = \boldsymbol{L}\boldsymbol{Q} + \boldsymbol{W}, \quad (10)$$

where $\boldsymbol{W}$ is the noise vector and its convariance matrix is $\boldsymbol{\Sigma} = E\boldsymbol{W}\boldsymbol{W}^{\mathrm{T}}$. Though noises are not limited

to random noises, some other kinds of noises are hard to simulate. So only random noises are to be considered here.

Equations (9) and (10) are typical ill-posed systems and their exact solutions $\boldsymbol{Q}$ do not exist; nevertheless their optimal pseudo-solutions still can be obtained to replace the real solutions and expressed as

$$\boldsymbol{Q} = \boldsymbol{L}^{+}\boldsymbol{B}, \tag{11}$$

where $\boldsymbol{L}^{+}$ is the pseudo-inverse matrix of $\boldsymbol{L}$, and there are many inverse algorithms to calculate $\boldsymbol{L}^{+}$, among which the Moore–Penrose inverse or the minimum-norm least-square (MNLS) method is the most basic approach. The optimal truncated pseudoinverse method (OTPIM), optimal weighted pseudoinverse method (OWPIM), optimal constrained linear inverse method (OCLIM), *etc.*[11,13,20] are also suitable for this inverse problem.

In the next section, we will adopt MNLS, OWPIM and OCLIM inverse methods to reconstruct the current dipole array based on the magnetic fields generated by current multipole model with considering boundaries of sub-conductors with different conductivities. The imaging effect and the noise-resistance of these three methods will be compared.

3. Simulation results

As shown in Fig. 1, a concentric ellipsoid heart-torso model is constructed by BEM to handle the influence of boundaries on magnetic field distribution. This model is composed of two concentric homogeneous parts: heart area (heart muscle) with conductivity σ_1 and the area between torso and epicardial surface (inner torso tissue) with conductivity σ_2, and simultaneously neglects other tissue effect. We adopt σ_1 and σ_2 to be 0.10 S/m and 0.04 S/m respectively.[21] The dot lines along the longitude and the latitude of the torso surface show how the surface is tessellated into small triangles. In this paper, the torso and the heart are both divided into 1104 triangles, accompanied with 554 nodes. The observation plane is placed in front of the torso (0.12 m away from the *xoy* plane) and the magnetic measurements are carried out at each node in this plane. There are 6×6 measuring points in all, and the nearest distance between two points is 0.04 m. Located inside the heart is the reconstruction plane (imaging plane), which is coincident with the *xoy* plane. There will be 14×14 reconstructing current dipoles scattered evenly on the reconstruction plane and the distance between the nearest reconstructed dipoles is set to be 0.005 m.

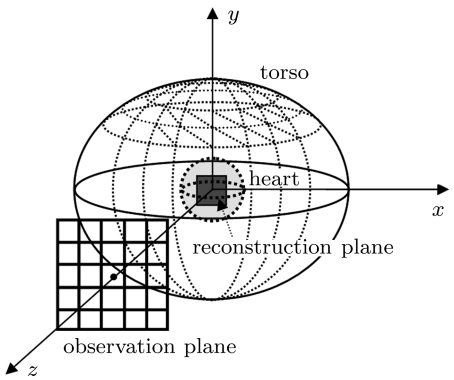


Fig. 1. Heart-torso model constructed by BEM. Dot lines along the longitude and the latitude of torso surface show how this model is tessellated. The observation plane is placed in front of the model. The reconstruction plane sits in the centre of heart model.

First, we discuss the simulated magnetic field distribution induced by the current multipole. The parameters of current multipole are chosen according to inverse calculation depending on realistic measurements, these being dipole moment $\boldsymbol{p} = (1,1,1)\mu\mathrm{A}\cdot\mathrm{m}$, magnetic dipole moment $\boldsymbol{m} = (0.1,0.1,0.1)\mu\mathrm{A}\cdot\mathrm{m}^2$, and five elements of quadrupole tensor $(A_{20},A_{21},B_{21},A_{22},B_{22}) = (0.1,0.1,0.1,0.1,0.1)\mu\mathrm{A}\cdot\mathrm{m}^2$. In view of these multipole parameters, the simulated MCG map in the measuring plane without and with considering boundaries are given in Fig. 2 respectively. After comparing Fig. 2(a) which shows the B_0 map, with Fig. 2(b) signifying B map, it is obvious that the influence from the surface currents due to the sudden change of conductivities in the interface does not change the shape of MCG map's contour but does change the magnetic field magnitudes, which are the same as what happen to the condition when the single current dipole is selected to be the cardiac functional current source. However, the degree to which B is counteracted is different. In single current dipole condition, the magnitude of B is about 1/3 that of B_0 at the same measuring point according to our previous study, while as to current multipole, B is much less offset by magnetic fields due to surface currents. Signs '+' and '–' denote areas of positive and negative magnetic fields respectively.

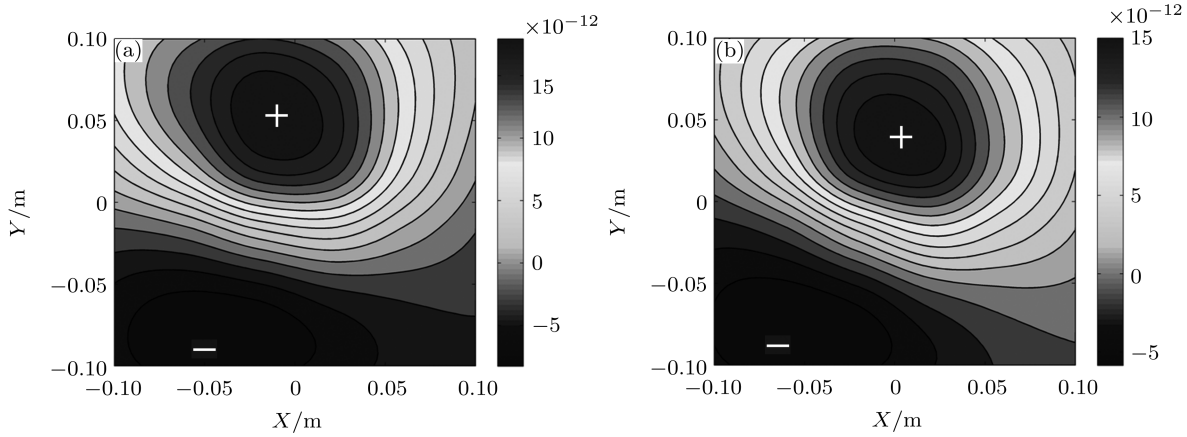


Fig. 2. MCG map without and with considering boundary effects: B_0 (a) and B (b). Sign '+' denotes the area of positive magnetic fields, and '–' represents the area of negative magnetic fields.

Then Fig. 3 shows the current dipole array reconstruction with using magnetic data given by Fig. 2(a). Figure 3(a) shows the two-dimensional (2D) dipole reconstructing pattern, where the distribution of current dipoles is roughly consistent with the magnetic field distribution in Fig. 2(a). Figure 3(b) indicates the three-dimensional (3D) current dipole array image. In reality, in the process of this image, some random noises have been added to simulated magnetic data. However, because the magnitudes of these noises is quite low, where the signal-to-noise ratio (SNR) is 172.54dB, there is little influence on imaging effect.

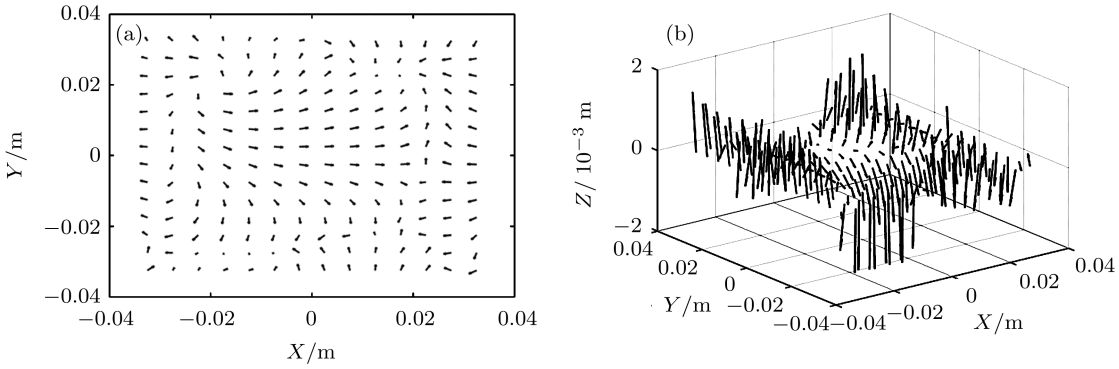


Fig. 3. Current dipole array 2D (a) and 3D (b) reconstructions.

Next, we consider the effects of three parts of current multipole expansion terms on magnetic field distribution separately, and the current dipole array imaging based on magnetic fields of the three parts in bounded space. Current multipole parameters remain the same and the SNR for magnetic imaging is also 172.54 dB. Figure 4(a) is for the leading term—current dipole MCG map, taken as inputs of current dipole array reconstruction shown in Fig. 4(b). Figures 4(c) and 4(d) show the magnetic dipole MCG map and its corresponding current dipole array reconstruction. Current dipoles shown in Fig. 4(f) are reconstructed by using magnetic data obtained from the current quadrupole model whose magnetic field distribution is given in Fig. 4(e). Signs '+' and '–' denote areas of positive and negative magnetic fields respectively.

In the procedure of measurements, detecting noises from external environments, measuring errors, and self-change of detected samples, or from any other possible sources, are inevitable and should be considered carefully to guarantee effective measurements and obtain valuable physiological activity information. Although there are many kinds of noises, some of which are difficult to simulate by computer, only the most common noise—random noise is to be discussed here. A random noise vector with mean zero is added to our program. The dipole array imaging effect as the function of SNR changes is inspected under different inverse methods (MNLS, OWPIM and OCLIM). Furthermore, two imaging parameters: the residual χ^2 ($\chi^2 = (\boldsymbol{B} - \boldsymbol{L}\hat{\boldsymbol{Q}})^{\mathrm{T}} E \boldsymbol{W}\boldsymbol{W}^{\mathrm{T}}(\boldsymbol{B} - \boldsymbol{L}\hat{\boldsymbol{Q}})$) and its mean value $\mathrm{E}\chi^2$, are given. The former parameter shows how closely the reconstructed field values

match the measured signals, and the latter parameter indicated how closely the reconstruction and the given measurements match on average.

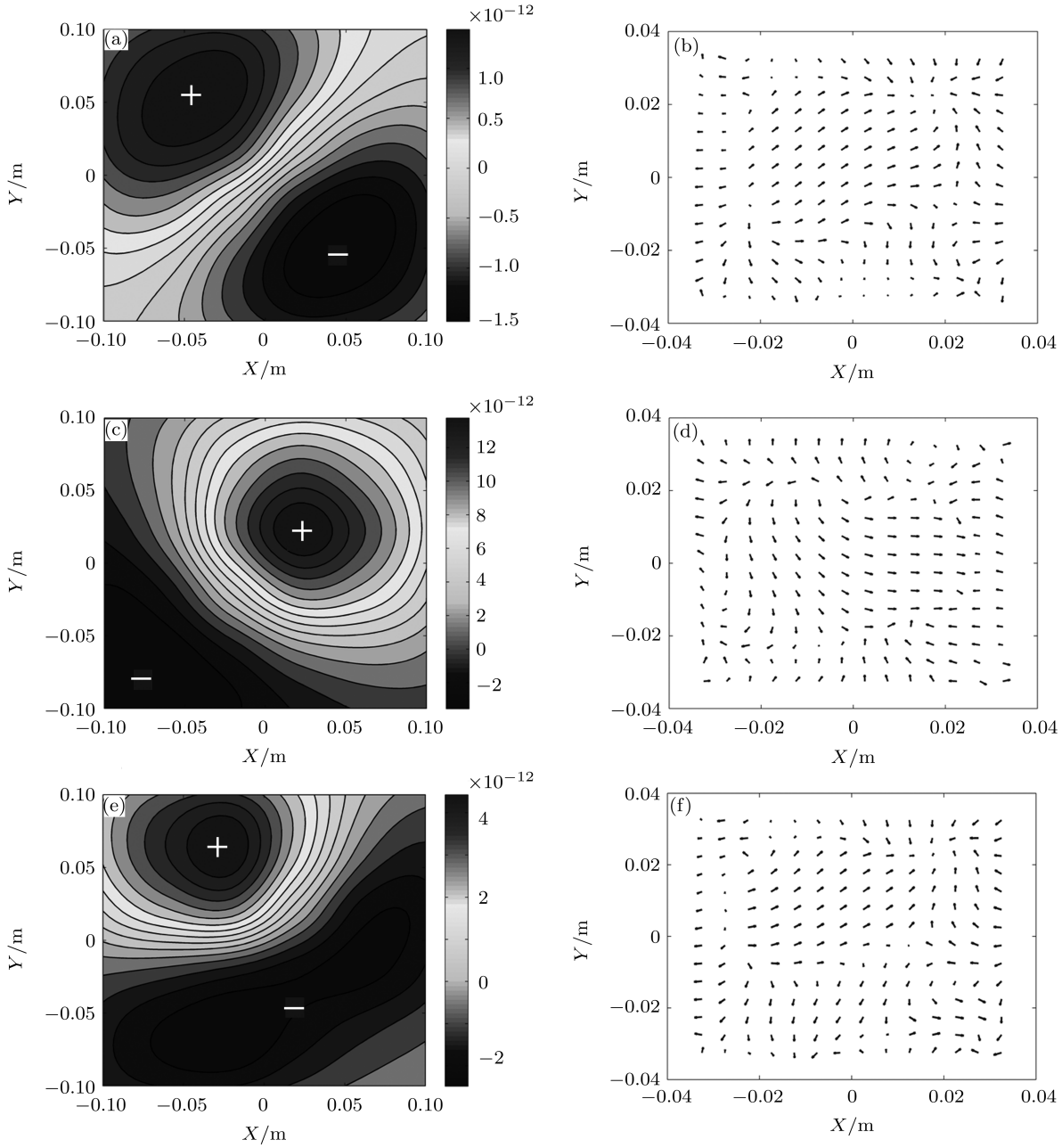


Fig. 4. Magnetic distributions and the current dipole array reconstructions based on current multipole expanded to the first order terms. Panels (a), (c) and (e) illustrate MCG map caused by current dipole, magnetic dipole and current quadrupole respectively, and based on these three kinds of magnetic fields, there are obtained panels (b), (d) and (f) expressing the corresponding reconstructed current dipole arrays. Sign '+' denotes the area of positive magnetic fields, and sign '–' represents the area of negative magnetic fields.

Figure 5 displays the reconstructed current dipole array maps with diverse SNRs using MNLS inverse method: –26.64 dB (a), –6.35 dB (b), 13.67 dB (c), 33.78 dB (d), 54.05 dB (e), 73.63 dB (f), 92.95 dB (g), and 113.42 dB (h). By examining the change of reconstructing effect with the increase of SNR, it is found that when SNR is more than about 55dB, the imaging effect becomes relatively ideal and this SNR threshold is approximately consistent with that in the condition studied before where the single current dipole served as a testing source.

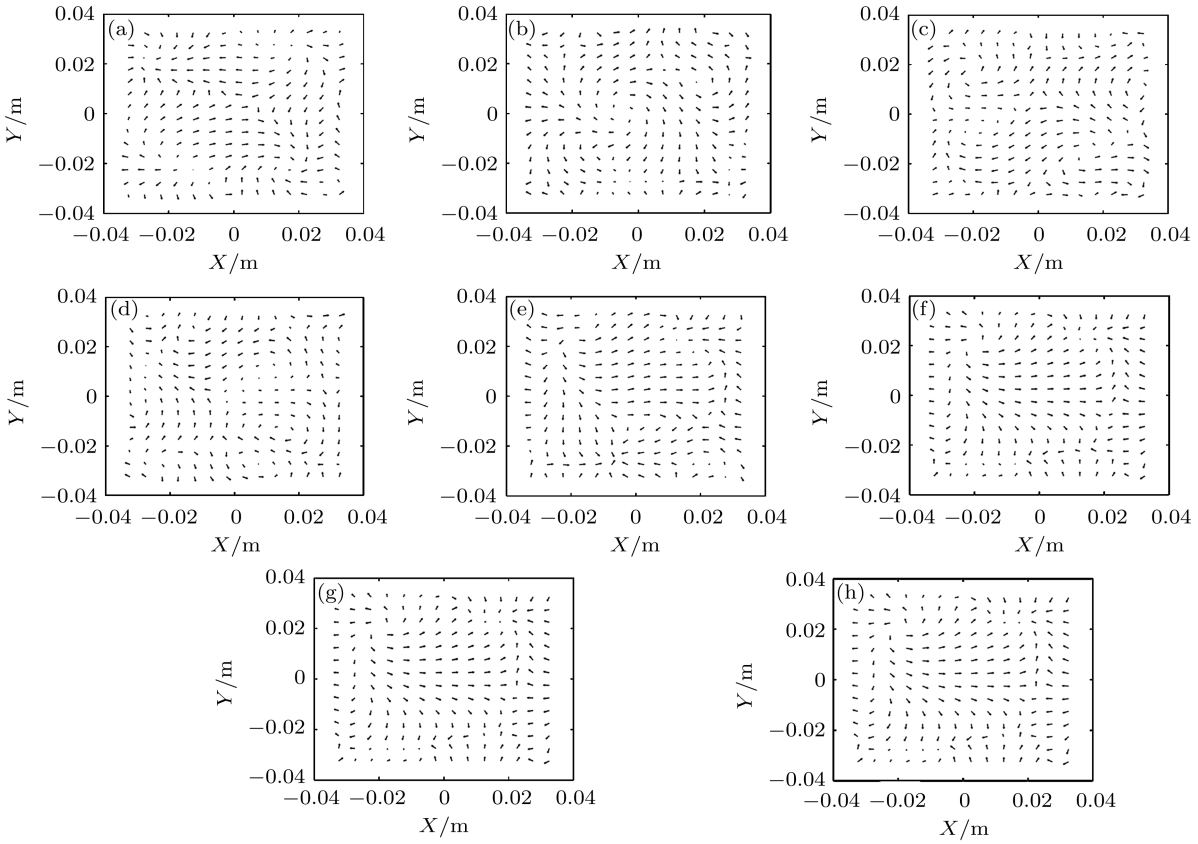


Fig. 5. Current dipole array reconstructions based on MNLS with different SNRs: –26.64 dB (a), –6.35 dB (b), 13.67 dB (c), 33.78 dB (d), 54.05 dB (e), 73.66 dB (f), 92.95 dB (g), and 113.42 dB (h).

Next, the reconstructing effects using MNLS, OWPIM and OCLIM inverse approaches are to be considered. After comparing the magnetic images from these three approaches, we realize that the OCLIM gives the best reconstructed current dipole array map and MNLS provides a better map than OWPIM at the same SNR, which can be clearly seen in Fig. 6. Figures 6(a), 6(b) and 6(c) represent current dipole array reconstructions adopting MNLS, OWPIM and OCLIM at SNR = 54 dB, respectively. Moreover, this advantage of OCLIM also exists when SNR > 54 dB. To some degree, this feature illustrates that the current dipole array reconstruction with employing OCLIM can resist random noises most powerfully.

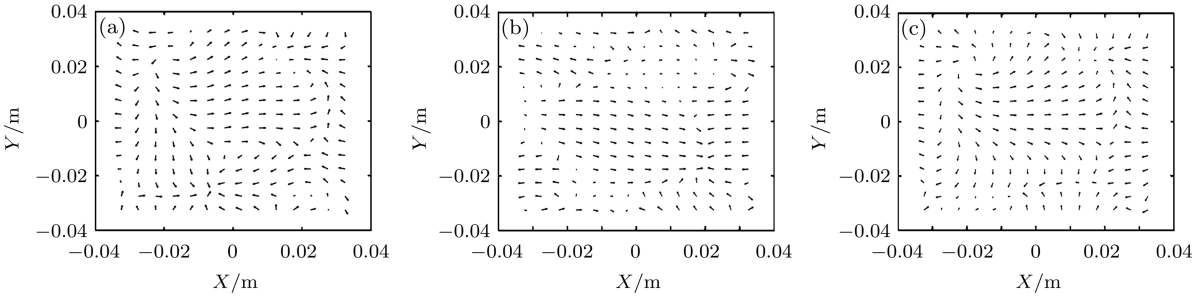


Fig. 6. Comparison among current dipole array reconstructions obtained from three inverse methods at the same SNR = 54 dB. Panels (a), (b) and (c) are based on MNLS, OWPIM and OCLIM, respectively.

To reflect imaging errors under diverse SNRs quantitatively, two reconstruction parameters are introduced: χ^2 and $E\chi^2$. Figure 7 signifies the curves for reconstruction residual χ^2 versus SNR. Lines with '$*$', '$\bigcirc$' and 'Δ' illustrate residual tendencies from MNLS, OWPIM and OCLIM inverse methods. Note that $\lg \chi^2$ serves as the scale of y axis. From this figure, the '$*$' line related to MNLS method possesses smaller χ^2 when SNR is lower and it increases approximately linearly after about 20 dB, before which χ^2s

are roughly the same. As to '◯' and 'Δ' lines, which are concerned with OWPIM and OCLIM, they decline before about 40 dB and 60 dB respectively, and then both ascend. The tendencies of χ^2 demonstrate that the degree to which the measured and the reconstructed fields match does not change monotonically with SNR.

Figure 8 shows the mean reconstruction residual $E\chi^2$ as a function of SNR. Lines with '*', '◯' and 'Δ' correspond to MNLS, OWPIM and OCLIM inverse methods. Figure 8(a) shows that the tendencies of $E\chi^2$ under three conditions are roughly the same, that is, $\lg E\chi^2$ decreases linearly with the increase of SNR after SNR $\approx$ 0 dB, which indicates that the average difference between the reconstructed magnetic fields and the measured magnetic fields decreases gradually with SNR increasing. To examine Fig. 8(a) more clearly, it is magnified as shown in Fig. 8(b). From Fig. 8(b) it follows that the $E\chi^2$ from the OCLIM is slightly less than those from the other two inverse methods.

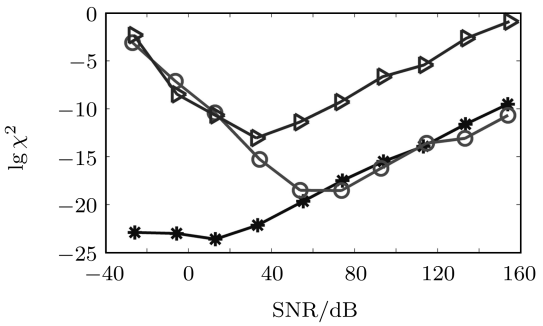


Fig. 7. Curves for reconstruction residual χ^2 versus SNR. Lines with '∗', '◯' and 'Δ' illustrate residual tendencies based on MNLS, OWPIM and OCLIM inverse methods. $\lg \chi^2$ serves as the scale of y axis.

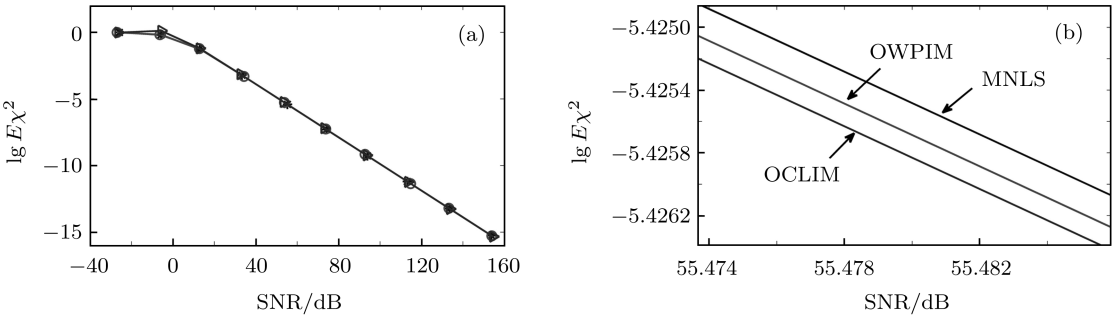


Fig. 8. Curves for mean reconstruction residual $E\chi^2$ versus SNR. Lines with '∗', '◯' and 'Δ' illustrate mean residual tendencies based on MNLS, OWPIM and OCLIM inverse methods. Panel (b) shows the magnified parts of panel (a). $\lg E\chi^2$ serves as the scale of y axis.

On account of the low values of χ^2 and $E\chi^2$, the inverse computations depending on MNLS, OWPIM and OCLIM inverse methods are all reliable.

By balancing the reconstructing effects of the current dipole array maps at the same SNR and the imaging parameters, OCLIM is an optimal option for magnetic source imaging based on current multipole model, nevertheless its advantages are not obvious compared with those of MNLS and OWPIM.

4. Conclusion

Making use of magnetic fields generated by current multipole expanded to the first order term as a testing source, in this article the cardiac functional current source (current dipole array) reconstruction is realized. Before the current source imaging, considering the boundary effect, the magnetic field distributions excited by three parts of first order expansion of multipole: current dipole, magnetic dipole and current quadrupole, are inspected and it is clear that the current multipole induced magnetic fields are not so greatly influenced by surface currents as the current dipole induced magnetic fields. Then, based on magnetic fields caused by current multipole, the corresponding current dipole array images are achieved by MNLS, OWPIM and OCLIM inverse methods separately. The distribution of current dipoles is consistent with magnetic field distribution.

As for measurement noises, random noises are added to simulated magnetic signals. Imaging effects based on MNLS inverse method under different SNRs are compared, and the result displays recon-

struction with SNR more than about 55 dB, leading to relatively ideal images. Three linear reconstruction approaches—-MNLS, OWPIM and OCLIM are employed to find an optimal method for current dipole array magnetic imaging. When random noises with the same SNR (SNR $\approx$ 54 dB) are added, reconstructions from different imaging methods embrace different imaging effects although this difference is not obvious. By comparison, the reconstruction using OCLIM gives the best current dipole array map and MNLS's map is slightly better than OWPIM's map at SNR$\approx$54dB, and these characteristics exist even though SNR is at a higher level.

Two imaging parameters (residual χ^2 and mean residual $E\chi^2$) each as a function of SNR are also discussed in this article. As to residual, the χ^2 of MNLS is smallest when SNR is lower, and the tendencies of $\lg\chi^2$ based on OWPIM and OCLIM are both not monotonic since they ascend from about 40 dB and 60 dB respectively, before which $\lg\chi^2$ descends. But for the mean residual, the trends of $E\chi^2$ from the three inverse methods are roughly the same, which means that the $\lg E\chi^2$ decreases linearly after about 0 dB. Although the magnetic reconstructions based on MNLS, OWPIM and OCLIM have discrepant imaging effects and their residuals and mean residuals hold different trends, in light of the low values of χ^2 and $E\chi^2$, these inverse computations are reliable.

References

[1] Ma P, Yao K, Xie F X, Zhang S Y, Deng P, He D F, Zhang F, Liu L Y, Nie R J, Wang F R, Wang S Z and Dai Y D 2002 *Acta Phys. Sin.* **51** 224 (in Chinese)

[2] Ma P, Yao K and Xie F X 2005 *Chin. Phys. Sci.* **51** 224 (in Chinese)

[3] Gao J, Yang T, Ma P and Dai Y D 2010 *Chin. Phys.* B **19** 067402

[4] Wang J Z, Williamson S J and Kaufaman L 1992 *IEEE Trans. Biomed. Eng.* **39** 665

[5] Wang J Z 1993 *IEEE Trans. Biomed. Eng.* **40** 387

[6] Garbor D and Nelson C V 1954 *J. Appl. Phys.* **25** 413

[7] Hamalainen M, Hari R, Illmoniemi R J, Knuutila J and Lounasmaa O V 1993 *Rev. Mod. Phys.* **65** 413

[8] Gonnelli R S and Agnello M 1987 *Phys. Med. Biol.* **32** 133

[9] Jerbi K, Mosher J C, Baillet S and Leahy R M 2002 *Phys. Med. Biol.* **47** 523

[10] Shepp L A and Vardi Y 1982 *IEEE Trans. Med. Imaging* **MI-1** 113

[11] Shim Y S and Cho Z H 1981 *IEEE Trans. Acoust. Speech Signal Process.* **29** 904

[12] Smith W E, Dallas W J, Kullmann W H and Schlitt H A 1990 *Appl. Opt.* **29** 658

[13] Hughett P 1995 *Annals Biomed. Eng.* **23** 506

[14] Morrison D F 1967 *Multivariate Statistical Method* (New York: McGrawHill) p58

[15] Geselowitz D B 1970 *IEEE Trans. Magn.* **MAG-6** 346

[16] Koch H and Haberkorn W 2001 *Phil. Trans. R. Soc. Lond.* A **359** 1287

[17] Barr R C, Ramsey M and Spach M S 1977 *IEEE Trans. Biomed. Eng.* **BEM-24** 1

[18] Hamalainen M S and Ilmoniemi R J 1994 *Med. Biol. Eng. Comput.* **32** 35

[19] Nenonen J T, Hamalainen M S and Ilmoniemi R J 1994 *Med. Biol. Eng. Comput.* **32** 43

[20] Jeffs B, Leahy R and Singh M 1987 *IEEE Trans. Biomed. Eng.* **34** 713

[21] Osama A M and Fuat G U 1993 *IEEE Trans. Magnet.* **29** 1403